Composites Part B 158 (2019) 328–338

Contents lists available at ScienceDirect

Composites Part B

journal homepage: www.elsevier.com/locate/compositesb

Strain hardening polypropylene fiber reinforced composite from hydrated ladle slag and gypsum

Hoang Nguyen[a], Paivo Kinnunen[a], Valter Carvelli[b], Mohammad Mastali[a], Mirja Illikainen[a,*]

[a] Fibre and Particle Engineering Research Unit, University of Oulu, Pentti Kaiteran katu 1, 90014, Oulu, Finland
[b] Department A.B.C., Politecnico di Milano, Piazza Leonardo Da Vinci 32, 20133, Milan, Italy

ARTICLE INFO

Keywords:
Recycling
Mechanical properties
Numerical analysis
Mechanical testing
Ettringite

ABSTRACT

The use of industrial by-products brings both economic and environmental benefits. Ladle slag (LS) from steel processes is a promising raw material and has been used as a precursor in a few studies. To better understand the benefits of LS mainly on mechanical behavior, in this investigation, an ettringite-based binder was produced from the hydration between LS and gypsum. The material was reinforced with 2% v/v high tenacity polypropylene (HTPP) fiber to attain a high performance fiber reinforced cementitious composite with pseudo strain hardening (PSH) behavior. In addition, results of FEM numerical analysis show the accurateness of an available constitutive model in predicting the mechanical response of the HTPP fiber reinforced hydrated LS composite. Additionally, the experimental results reveal that using HTPP fiber greatly enhanced the mechanical properties of the hydrated LS. Moreover, PSH behavior and eventually multiple fine cracks were recorded by the digital image correlation (DIC) technique under uniaxial tensile tests. The numerical simulations show the capability of the concrete damage plasticity (CDP) model to predict the nonlinear behavior of the material with a good agreement between experimental and numerical predictions.

1. Introduction

Ladle slag (LS), a by-product from steel manufacturing processes, has shown promise as a precursor for cementitious materials. There are 2.1–2.6 million tons of LS produced in Europe annually if every ton of crude steel produced results in 12–15 kg of unrecycled LS according to a statistical report from the World Steel Association [1]. Therefore, LS is an interesting source to use in manufacturing inorganic binders with considerable environmental related benefits. In the literature, LS has shown its potential to be used as a precursor for cementitious materials [2]. In addition, LS was activated by an alkali solution to form an inorganic binder that attained up to 70 MPa compressive strength [3]. LS was also successfully used in Ref. [4] to produce an environmentally friendly cementitious materials for high-temperature applications.

Ettringite-based binders are a promising alternative to ordinary Portland cement (OPC). The main phase in the binders is ettringite, which is formed by chemical reactions between solid calcium alumino and calcium sulfate sources [5,6]. The most popular ettringite systems are calcium sulfoaluminate belite cement (CSAB) and supersulfated cement (SSC), which they can be produced from by-products, such as fly ash and blast furnace slag [5,6]. These residue-based binders reduce CO_2 emissions and offer comparative mechanical properties to OPC. Furthermore, the ettringite system leads to interesting characteristics such as high chloride resistance and heavy metal immobilization, as reported in Refs. [7,8]. In Ref. [9], LS was successfully used as a precursor to produce an ettringite system through reactions with dehydrated gypsum ($CaSO_4$). Although the material showed promising properties (e.g., over 1.5 h in initial setting time, roughly 45 MPa in compressive strength), the preparation process was sub-optimal, as it necessitated uneconomical steps such as re-melting and rapid cooling of the slag.

There is a lack of studies on high performance fiber reinforced ettringite-based binders. Similar to other inorganic binders, the ettringite systems exhibit a brittle mechanical behavior. By using fibrous reinforcement, the cementitious materials can improve the ductility under fiber bridging action, affecting the hardening and softening phases. This is, on one hand, a well-studied behavior for fiber reinforced OPC based materials with many reports on pseudo strain hardening (PSH) (i.e., strain hardening behavior of the brittle matrix attained by fibrous reinforcement) cementitious composites (i.e., ECC) [10–12]. On the other hand, there are no investigations in the literature on the mechanical properties of PSH cementitious composites with ettringite-based binders. In 2015, Jewell [13] studied the interfacial bond between different types of fibers and CSAB cements; since then, there

* Corresponding author.
E-mail address: mirja.illikainen@oulu.fi (M. Illikainen).

https://doi.org/10.1016/j.compositesb.2018.09.056
Received 17 January 2018; Received in revised form 27 August 2018; Accepted 21 September 2018
Available online 24 September 2018

have not been any further investigations on the macro scale mechanical properties of those composites. Thus, there is a need to study fiber reinforced ettringite-based binders, especially when the material offers more environmental benefits than conventional cements.

This investigation is encouraged by the lack of information about high performance fiber reinforced ettringite-based binders, as mentioned. This is the first attempt to produce PSH behavior on a cementitious composite from LS, gypsum, and high tenacity polypropylene (HTPP) fiber. The matrix is formed by the hydration between LS and gypsum (LSG). Compared to the hydrated LS in Ref. [9], this matrix provides more economic benefits by using the natural cooling process for LS and consuming less energy by using hydrated gypsum. As for the reinforcement, in a previous study [14], polypropylene fiber was effectively used to produce PSH behavior on alkali activated LS. As reported in Ref. [14], the fiber offers good mechanical properties and better cost efficiency than other commonly-used fibers (e.g., PVA fibers) when it comes to high performance cementitious composites. Consequently, the mechanical behavior of the HTPP fiber reinforced LSG is experimentally investigated for the following relevant properties: flexural strength, compressive strength, fracture toughness, and uniaxial tensile behavior.

Finally, numerical simulations are detailed in this study using finite element method (FEM) to assess the capability of a constitutive material model to capture the mechanical behavior of HTPP fiber reinforced LSG. In the numerical simulations, some unknown parameters of the concrete damaged plasticity (CDP) model [15], generally adopted for OPC concrete, were identified by conducting an inverse analysis. The numerical results were verified by the experimental results obtained from a mode I fracture. The comparison of the numerical simulations and the experimental results highlights the effectiveness of the CDP in commercial FEM software for modeling the mechanical properties of fiber reinforced ettringite-based binders. The numerical simulation findings contribute to the general knowledge about high performance fiber reinforced cementitious composites and HTPP fiber reinforced LSG.

2. Materials and methods

2.1. Materials

The LS was supplied by SSAB Europe Oy, Finland, while fine sand (FS) was milled from standard sand (DIN EN 196-1 [16]). The as-received slag was collected at the by-product cooling pit of SSAB Europe Oy, and the material was exposed to natural weathering. The chemical composition of the LS, as shown in Table 1, was analyzed by X-ray fluorescence (XRF) (PANalytical Omnian Axiosmax) at 4 kV. The free CaO measured by the method described in the standard EN 450-1 [17] was zero. As detailed in the previous study [14], particle size plays an important role in the activated reaction and the mechanical performance of the cementitious composite. Consequently, the as-received LS and FS were separately milled with a ball mill (TPR-D-950-V-FU-EH by Germatec, Germany) to reach a d50 value of less than 10 and 200 μm, respectively. The particle size distribution was then analyzed by a laser diffraction technique (Beckman Coulter 13 320) using the Fraunhofer model [18].

Gypsum was used as a calcium sulfate source in this study. The gypsum was $CaSO_4.2H_2O$ (cement nomenclature: $C\bar{S}.2H$) supplied by VWR Finland (product code 22451.360). In Ref. [9], $CaSO_4$ was used to react with rapid air cooled LS to form ettringite in its structure. In contrast, in this experimental investigation, hydrated gypsum (calcium sulfate dihydrate $CaSO_4.2H_2O$) was employed to take advantage of its availability in secondary resources. Also, using hydrated gypsum reduces the energy consumption on the dehydration in comparison to dehydrated gypsum (calcium sulfate $CaSO_4$). The particle size distribution of gypsum was measured by the same equipment and technique with LS and FS, and the median particle size d50 was 11.5 μm. Furthermore, the gypsum chemical component was analyzed by XRF, and the percentage of oxides in gypsum is indicated in Table 1. The mechanism and reactions to form ettringite are detailed in Section 2.2.

Table 1
Chemical composition (wt %) of LS and gypsum measured by XRF.

Oxide	CaO	SiO_2	Al_2O_3	Fe_2O_3	MgO	SO_3	Others
LS	50.96	8.27	27.87	1.13	6.31	0.80	4.66
Gypsum	41.40	0.96	0.12	0.07	0.48	53.75	3.22

Citric acid (product code C1949 by Tokyo Chemical Industry Co., Ltd., Japan) was used as a retarder for the LSG in this investigation. Citric acid has been proven to be an effective retarder in ettringite systems (see Refs. [19,20]), influencing the ettringite formation during hydration reaction [20]. Moreover, citric acid was also used in Refs. [21,22] as a retarder in gypsum plaster to improve setting time and workability. The acid prevents the nucleation and the subsequent crystal forming process of ettringite, as proposed in Ref. [23]. Automatic Vicat machine (model E044N by Matest, Italy) was employed to record the setting time of mortars, complying with ASTM C191-13 [24]. Based on the preliminary experiments in this investigation, 1.8% citric acid solution was used to attain the initial setting time of almost 1.2 h.

Polypropylene (PP) fiber was used in previous studies to attain strain hardening behavior on cementitious composites [12,14]. In this investigation, HTPP fiber was provided by Brasilit (Saint Gobain, Brazil). The mechanical and physical properties of fiber are listed in Table 2. While HTPP fiber is inexpensive compared to PVA fibers because of the worldwide availability of PP raw material [25], the fiber offers good mechanical properties due to the high tenacity from manufacturing processes. Consequently, using PP fiber is more cost efficient than other polymeric fibers used in ECC (e.g., PVA and high modulus polyethylene fibers). The adopted HTPP fiber was successfully used to produce strain hardening OPC based cementitious composites [25]. According to the design framework in Refs. [11,26] and our preliminary experimental results, the minimum volume fraction of fiber of 2% was chosen to yield PSH behavior on HTPP fiber reinforced LSG composites with adequate workability. The same fiber volume fraction was also effectively used in Ref. [25] for HTPP fiber reinforced ECC.

2.2. Hydration of ladle slag and gypsum

The main reaction product of LSG is ettringite, and it is also the dominant phase in CSAB and SSC cements [27–29]. Mayenite ($C_{12}A_7$) is the main mineral in LS, as indicated by the X-ray diffraction (XRD) results (Fig. 1). The mineral tends to have a rapid reaction with water to produce hydrogarnet (C_3AH_6) aluminum hydroxide (AH_3) as follows [9]:

$$C_{12}A_7 + 51H \rightarrow 6C_2AH_8 + AH_3 \rightarrow 4C_3AH_6 + 3AH_3 + 18H \quad (1)$$

Hydrogarnet prevents further reactions of $C_{12}A_7$ and consequently impedes any further strength development in the hydrated LS. By adding gypsum, the system forms ettringite ($C_3A.\ 3\bar{C}S.\ 32H$) instead of hydrogarnet after the chemical reaction between $C_{12}A_7$ and gypsum; the reaction is as follows:

$$C_{12}A_7 + 12\bar{C}S.\ 2H + 137H \rightarrow 4C_3A.\ 3\bar{C}S.\ 32H + 3AH_3 \quad (2)$$

The XRD pattern of LSG in Fig. 1 clearly shows that ettringite is the dominant phase in the structure. Ettringite was estimated to be roughly 65% of the crystals in the LSG. Therefore, the mineral is the main strength-giving phase of LSG, which is discussed in more detail in Section 3.2.

The required amount of gypsum to complete the reaction $C_{12}A_7$ entirely was calculated by the modified Bogue equation, as proposed in Ref. [9]. The amount of oxides from XRF analysis (see Table 1) was used

Table 2
Mechanical and physical properties of HTPP fiber.

ID	Type	Young's modulus (GPa)	Elongation at break (%)	Tensile strength (MPa)	Length (mm)	Diameter (μm)	Density (g/cm^3)
HTPP	Multi-fiber	9	22	910	10	12	0.91

to calculate the percentage of C_4AF, $C_{12}A_7$, and C_2S in the LS. More details about the calculations and modified Bogue equations can be found in Ref. [9]. The percentage of $C_{12}A_7$ in the LS was approximately 47.5%; therefore, the gypsum-to-LS ratio to complete the hydration of LS was roughly 0.38. However, the dosage of 30% gypsum was recommended as an optimized amount after the experimental investigation in Ref. [9] due to crack formation at 20% and 40% gypsum dosage.

2.3. Fiber reinforced mortar preparation

The preparation of mortar specimens proceeded as follows: citric acid solution was prepared with a concentration of 1.8%; citric acid solid was weighted and dissolved into water by using magnetic stirring with speed 250 rpm for 30 min. The solution was kept at room temperature (roughly 23 °C). LS, gypsum, and FS were then weighted and mixed in a 5-L Kenwood mixer at low and high speed (70 rpm and 150 rpm, respectively) for 1 min at each level. The citric acid solution was added gradually to the dry mixture. The mortar was mixed at low speed for 3 min before adding the PP fibers into the mixture. The fibers were added gradually to the mortar to obtain uniform fiber distribution and to prevent fiber clustering during mixing. During the process, the mixing speed was kept at low level and the mortar was checked periodically to ensure a uniform fiber dispersion in the mortar. After adding the fibers, mixing was continued for 10 min at high speed. It took approximately 20–25 min to complete the mixing process. Mortar samples were cast into molds and vibrated for 3 min at a frequency of 1 Hz. Samples were cured in plastic bags at room temperature for 24 h before demolding. Samples were cured in a water bath at room temperature (approximately 23 °C) until testing (7 and 28 days). The recipe of the mixture is shown in Table 3.

A superplasticizer and dispersing agent were employed to gain proper workability and fiber dispersion. The superplasticizer was a melamine based chemical specified for calcium sulfate cements; the chemical was powdered Melment F10 provided by BASF (Germany).

Table 3
Mix proportions of the LSG reinforced with HTPP fiber.

Sample ID	Slag	Gypsum	Sand	Citric acid[a]	W/B[b]	PP fiber	Fiber volume fraction
2PP-LSG	0.7	0.3	0.5	1.8%	0.45	HTPP	2%

[a] Citric acid mixed with water to produce solution with 1.8% concentration.
[b] W/B (water-to-binder ratio) with total binder mass by the sum of the mass of slag and gypsum.

The dispersing agent was sodium polymethacrylate (commercial name Darvan 7-N) supplied by Vanderbilt (USA) in liquid form. The role of the agent is to stabilize the viscosity and rheology of the mortars and to ensure proper fiber distribution in mortars [30,31]. The dosage of the superplasticizer and dispersing agent were 0.5% and 1%, respectively, by weight of total binder mass. The former was dry-mixed together with LS, FS, and gypsum, while the latter was stirred well into the citric acid solution.

3. Mechanical experiments

3.1. Experimental procedures

The effects of HTPP fiber reinforcement on LSG were measured considering some main mechanical properties, including flexural, compressive, tensile strength, and fracture toughness. These properties can provide a clear understanding on the performance of HTPP fibers reinforced LSG.

Uniaxial tension and flexural (notched and un-notched beams) tests were assisted by digital image correlation (DIC) techniques to monitor the crack patterns. Images were captured and analyzed by LaVision StrainMaster [32] and VIC-2D [33]. The image acquisition frequency was set at 1 Hz, and the speckle pattern region of the sample was illuminated by an LED light source. The aperture and the shutter speed of

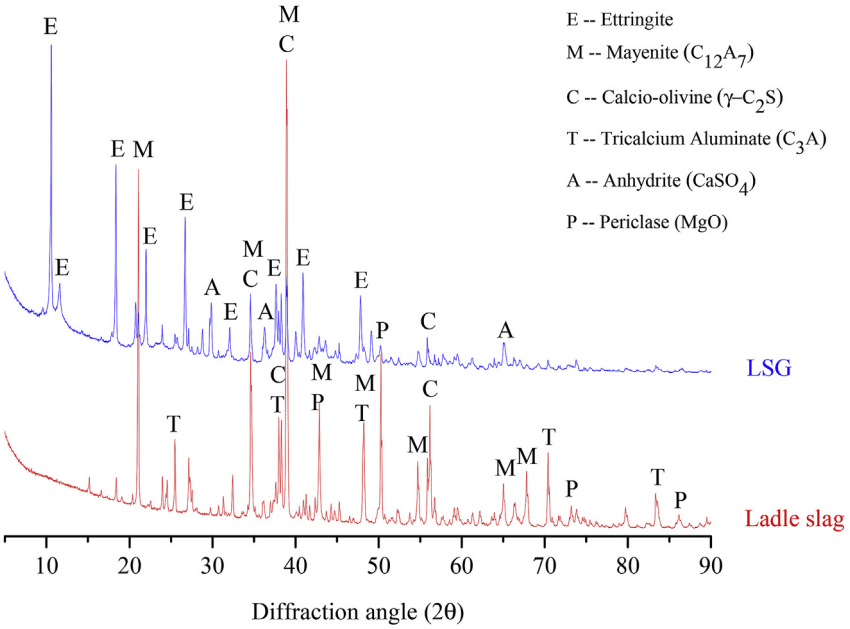

Fig. 1. XRD characterization of hydrated ladle slag and gypsum compared to as-received ladle slag.

camera were set to f/4.0 and 2000 μs, respectively. Post processing of images allows measurement of the full-field displacement and calculation of the strain distribution over the surface previously speckled with black and white acrylic paints. Some of the adopted parameters for correlation were subset size 37 and step size 3. Those were selected because lower values of subset and step sizes did not generate considerable variation of the calculated strain field.

The three-point bending for un-notched specimens and compressive strength tests, according to the standard ISO 679-2009 [34], were conducted by a Zwick device (load cell of 100 kN). After 7 and 28 days of curing in a water bath at room temperature, four specimens for each of the considered materials were tested by the three-point bending test. The purpose was to determine the flexural characteristics of the reinforced mixtures compared to the reference unreinforced material. The three-point bending test was done using displacement control and a speed rate of 0.4 mm/min. The compressive strength was measured by loading halves of the prismatic bending specimens. At least six specimens were tested for each combination and each curing time, and the displacement speed was set to 1 mm/min.

The fracture toughness was investigated by the three-point bending test while loading the notched specimens according to RILEM 1985 TC50-FMC [35]. Fig. 2 shows the scheme of the three points bending test and the geometry of the notched specimen. The notch width was 1 mm. The three-point bending test was conducted after 28 days curing in water at room temperature by the same loading device for the bending tests. The displacement-loading rate was 0.4 mm/min. Fracture energy was calculated based on the strategy used in Ref. [35], while the fracture toughness was computed by the effective crack model suggested by Karihaloo and Nallathambi [36].

Uniaxial tension tests were then performed on dog-bone specimens with dimensions recommended by Japan Society of Civil Engineers for high performance fiber reinforced cement composites [37]. The adopted main geometrical features according to [37] were the following: width at the grip zone was 60 mm, width of the free length was 30 mm, thickness was 13 mm, total length was 330 mm, and the free length was 80 mm. The specimen geometry was successfully used in previous investigations in the literature (e.g., [38]). In addition, the tensile tests of specimens cured in water for 28 days were performed with a machine MTS 810 (maximum load capacity of 10 kN) with a loading rate of 0.5 mm/min as in Ref. [38].

3.2. Results and discussions

The experimental results provided an overview on the modification of some mechanical properties of the cementitious composite from LSG mortars and HTPP fiber. The effect of the fibrous reinforcement was analyzed by observing the fracture surface of the bent specimens with a scanning electron microscope (SEM). Additionally, flexural tests clarified the role of fibrous reinforcement on the crack initiation and propagation by the DIC technique. Finally, the strain hardening behavior of the developed composites was analyzed under uniaxial tensile load, and the crack propagation was monitored by the DIC technique as in Ref. [38]. Experimental results revealed that the HTPP fibers offered considerable improvements in the mechanical properties of LSG composite under different loading conditions. Moreover, the PSH behavior was recorded during uniaxial tensile tests with the appearance of multiple cracks.

3.2.1. Bending

The flexural strength of reinforced material was considerably improved compared to the plain material. Fig. 3a shows the flexural properties of the mixtures. The increase ranged approximately from 60% to 130% after 7 and 28 days, respectively, of curing for 2PP-LSG. In the literature [39,40], the negative effects of PP fibers, due to weak bond between PP fibers and its surrounded matrix, and the debonding process from the matrix [39], were reported on the long-term flexural strength of fly ash and slag based geopolymer, while there was a negligible effect on the early ages. The better flexural performance of HTPP fiber reinforced material in this investigation is mainly connected to the high tenacity of fibers that have high stiffness and high tensile strength, allowing for a better load-carrying capacity between matrix and fibers. Also, due to the high-early-strength nature of the ettringite system [27,28], there was no difference in flexural strength of 2PP-LSG at 7 and 28 days when the fibers and the matrix were already well-bonded.

The HTPP fiber changed the crack patterns of LSG composite completely with deflection hardening behavior recorded by DIC. Stress vs. mid-span deflection curves of the reinforced (2PP-LSG) and unreinforced (LSG) materials are compared in Fig. 4, and the curves were plotted by calculating the vertical deflection of samples with the DIC technique. The plain material showed a typical brittle failure after reaching peak load, while the 2PP-LSG exhibited deflection hardening behavior with a significant increase of load after the onset of initial crack. The fundamental requirement for strain-hardening behavior is the occurring of steady-state cracking under tensile load via the load transferring between fibers and matrix, as reported in Ref. [10]. Under fiber bridging action, the fibers delayed the formation of crack localization and the sudden failure of the brittle matrix. These results are consistent with literature findings with PP fiber reinforced OPC composites. Deflection hardening behavior has been observed with 2% v/v PP fiber in concrete [41], while with a PP fiber volume fraction of 0.5%, the composite exhibits strain softening behavior [42]. Beside the positive effect of fiber bridging action, the results show that adding HTPP fibers increased the crack tortuosity, prolonged crack formation, and absorbed more energy [43]. At a mid-span deflection of 2 mm, the residual flexural strength was approximately 35% of the flexural strength.

The HTPP fibers and the LSG matrix were properly bonded, improving the bridging capacity of the fibers. Along with deflection hardening behavior, multiple cracks were generated on 2PP-LSG, as observed by the DIC (Fig. 5). After the initial crack, the fibers transferred tensile load across the fracture surface, slowing the rate of additional crack formation. The stress-transferring process was continued until the fibers were pulled out, as exhibited by the softening branch on

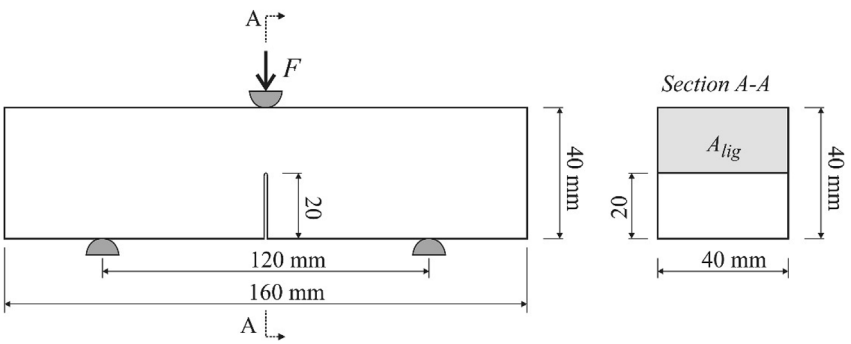

Fig. 2. Scheme of the notched prismatic beam for fracture toughness test (mode I).

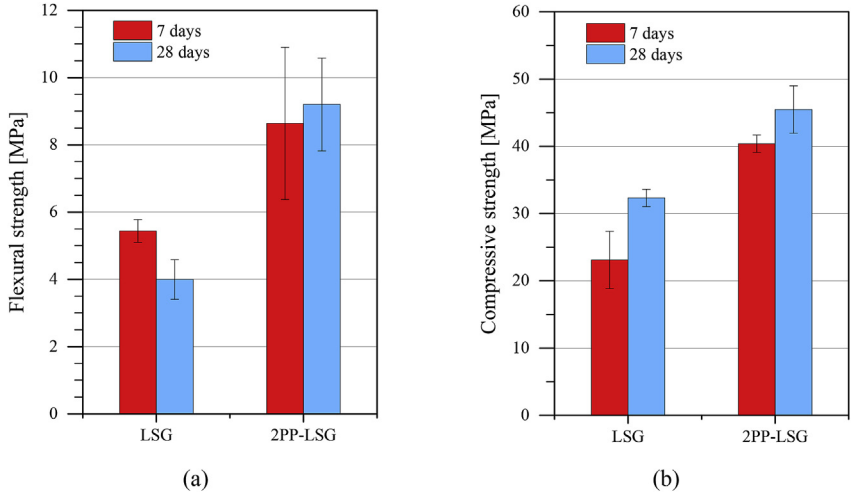

Fig. 3. (a) Flexural and (b) compressive strength of materials after 7 and 28 days of curing.

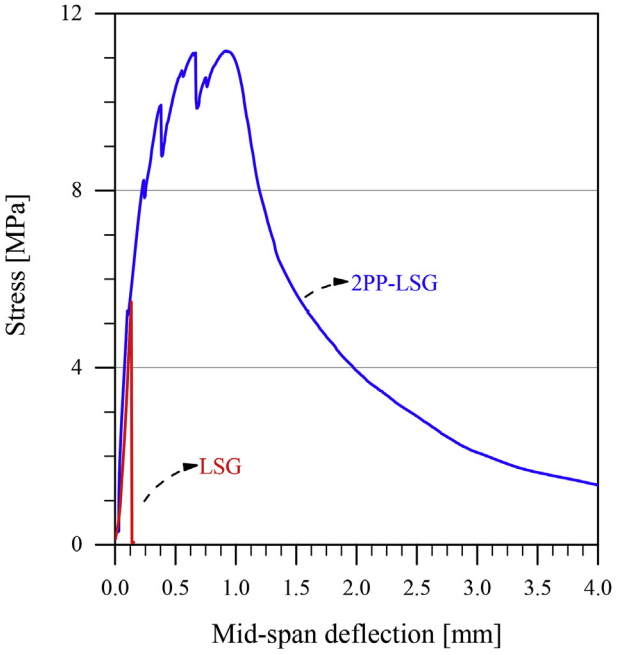

Fig. 4. Flexural tests: representative load vs. mid-span deflection curves measured by DIC.

the stress vs. mid-span deflection of 2PP-LSG (see Fig. 4). In contrast, there was only one localized crack recorded on the plain material by DIC image. The crack indicated the brittle failure of LSG, in which the load level dropped suddenly after reaching peak load (see Fig. 4).

The effect of fibers led to a larger deformation of the specimens with relevant increase in the failure mid-span deflection under three-point bending load. The local influence of the fibrous reinforcement on LSG was captured by SEM images on the fracture surface (Fig. 6). The fracture surface of reference material exhibited typical brittle failure with crack propagation along interfacial transition zone between LSG and FS (see Fig. 6a). The SEM images also show that the main phase in LSG is ettringite generated from the chemical reaction with $C_{12}A_7$ (see Equation (2)). The SEM images of the 2PP-LSG (Fig. 6b) clearly show that HTPP fibers dominantly failed by de-bonding. Furthermore, the dispersed fibers had some residual mortar still in adhesion, showing a good bonding between fibers and LSG matrix. The good bonding strength consequently led to an efficient load carrying capacity at the macro scale, as highlighted in Figs. 4 and 5. Hence, higher energy was spent on de-bonding and pulling out fibers. The 2PP-LSG absorbed a much larger amount of energy for propagating cracks, resulting in a high ductility. The latter could be measured by the ductility index μ (ratio of the ultimate hardening deflection to the deflection corresponding to the crack initiation) that is for the present reinforced materials μ ≈ 5, while a PAN fiber (4% v/v) reinforced OPC composite attained μ ≈ 8, as reported in Ref. [44].

3.2.2. *Unconfined compression*

The reinforced material exhibited a higher compressive strength than the plain material at both early and final ages. Fig. 3b shows an increase by approximately 75% and 40% in the 2PP-LSG after 7 and 28 days of curing, respectively, compared to the plain mixture. Using the HTPP fibers increased the compressive strength, contradicting findings reported in literature [40,45]. In general, high performance fiber reinforced cementitious composites show higher compressive strength than the unreinforced materials [46]. However, if the bonding strength between fibers and concrete is weak, adding more fibers into the matrix decreases the compressive strength [45]. Additionally, fibers with different mechanical and physical properties can affect the debonding and frictional pull-out behavior [47]. The HTPP fibers delayed the localization of the macro cracks and the propagation of micro-cracks [43]. Therefore, the driving force for the cracks is curtailed [48]. Therefore, it

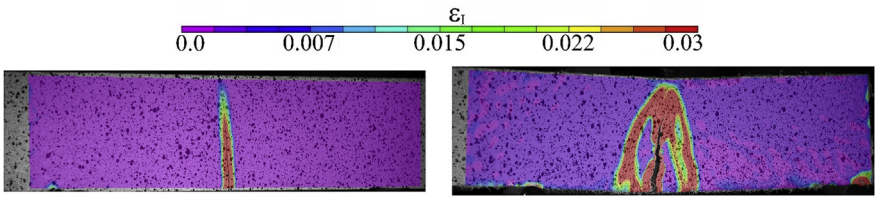

Fig. 5. Contour of the maximum principal strain by DIC at the maximum bending load of (a) LSG, (b) 2PP-LSG after 7 days of curing.

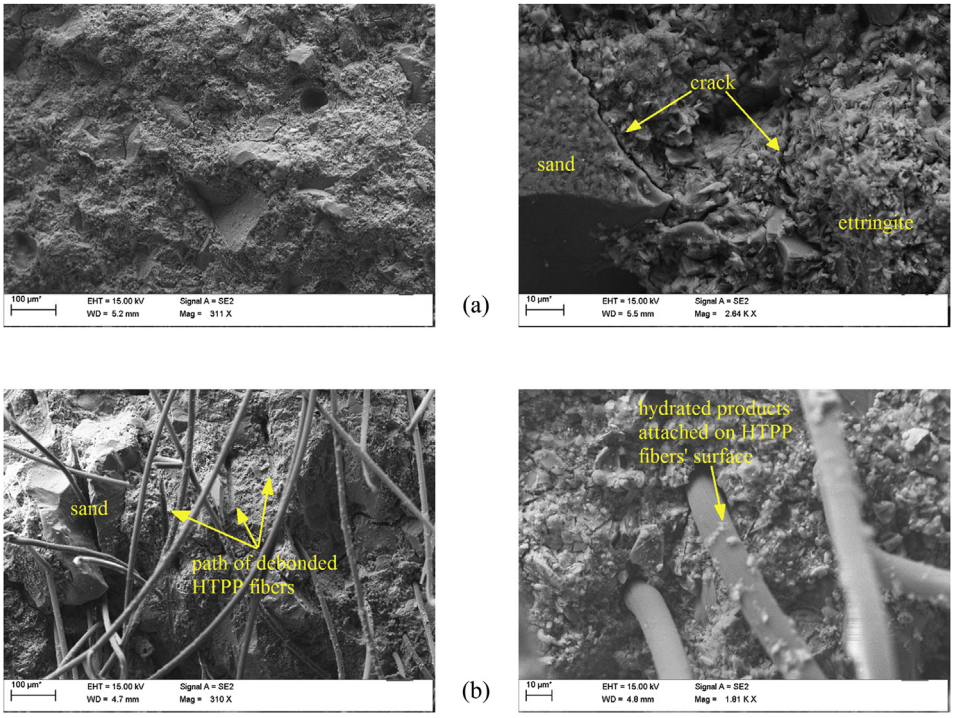

Fig. 6. Flexural tests: SEM images on fracture surfaces of (a) LSG and (b) 2PP-LSG specimen.

can be seen that the HTPP fibers bonded properly with LSG matrix, hence increasing the compressive strength of the composite.

Similarly to other ettringite systems (e.g., CSAB and SSC [5,6]), LSG can reach high strength at an early age. As reported in Ref. [27], gypsum was usually spent rapidly on the initial 16 h of hydration processes to form ettringite. Consequently, the material can gain high early strength within 7 days after the hydration; in Ref. [9], hydrated LS gained roughly 85% of its ultimate strength within 7 days. Fig. 3b shows that the compressive strength of LSG after 7 days of curing reached roughly 23 MPa, which is equivalent to 60% of the compressive strength (i.e., 33 MPa) at the final age. Therefore, in the present LS based ettringite system, the binder developed compressive strength for a longer time than other similar ettringite systems thanks to the form of gypsum used ($CaSO_4.2H_2O$). In comparison to Portland cement, where the main bonding phase is C-S-H, ettringite is the main strength-giving phase in LSG. Interestingly, as reported in the literature, using ettringite leads to the capability to capture heavy metals [7,8] and lower drying shrinkage [49] compared to the conventional cement.

The LSG binder tends to become more brittle in time. The behavior was highlighted in flexural and compressive strength of LSG (reference material) in Fig. 3. After 28 days of curing in water, the compressive strength increased by 40% compared to the 7-day-curing sample and reached 33 MPa. However, at the same time, the flexural strength of the composite decreased by approximately 25%. As discussed in Ref. [50], the compressive strength of ettringite-based binders may vary depending on the sulfate source (e.g., anhydrite, gypsum, or basanite). In LSG, ettringite was formed continuously during the curing period of 28 days; as a result, the compressive strength increased over time. However, the flexural strength decreased because, as reported in Ref. [51], the needle-shaped crystal might influence the formation of cracks, which can lead to a reduction in modulus and hardness. Therefore, further investigation on the micro-mechanical properties of LSG is warranted. Interestingly, no such difference was recorded on the fiber reinforced composite presumably due to good fiber bridging action, which curtailed crack propagation.

3.2.3. Fracture toughness

The plain composition showed typical brittle mode I fracture process under flexural loading, while the reinforced LSG had much better load-carrying capacity due to the fiber bridging action. The representative load-crack mouth opening displacement (CMOD) curves of materials obtained from DIC are compared in Fig. 7. The addition of HTPP fibers dramatically improved the peak and post-peak load levels with large CMOD. In agreement with a previous study on fiber reinforced cement mortars [52], the three main stages of material response under fracture toughness mode I are visible: initial crack appearance, minimum post-cracking load, and maximum post-cracking load. The crack propagated on 2PP-LSG early, but the HTPP fibers started bridging and absorbing energy immediately after the onset of initial crack. The material behavior is comparable to the split-film PP fiber reinforced alkali-activated LS [14]. Strain maps calculated by DIC at the peak load of two materials (points A and B) exhibited the large CMOD of 2PP-LSG compared to the plain material. At the peak load of the plain composition (point A), the crack propagated quickly with a low load level (approximately 336 N). Consequently, the composition exhibited a typical brittle failure in which the load level suddenly dropped with a low CMOD. The strain map of 2PP-LSG at peak load (point B) shows higher load-carrying capacity thanks to the effect of the fiber bridging action; the maximum load level was 961 N. Additionally, the crack mouth opened widely with roughly 0.6 mm in comparison to a CMOD of 0.008 mm of the reference material.

Flexural loading of notched beams revealed important improvements in the fracture energy and fracture toughness of the composite offered by the HTPP fibers. The quantitative improvements are represented in Fig. 8 with fracture energy and fracture toughness calculated based on the RILEM recommendation [35] and the effective crack model [36], respectively. The comparison in Fig. 8 indicates that the average fracture energy and fracture toughness of 2PP-LSG is 124.8 and 5.30 times larger than the reference material, respectively. In the literature, there are few investigations on the fiber reinforced ettringite systems (e.g., CSAB and SSC cements). Therefore, further studies on the interaction between fibrous reinforcement and ettringite systems and the effect of different fibers on fracture mechanism are necessary.

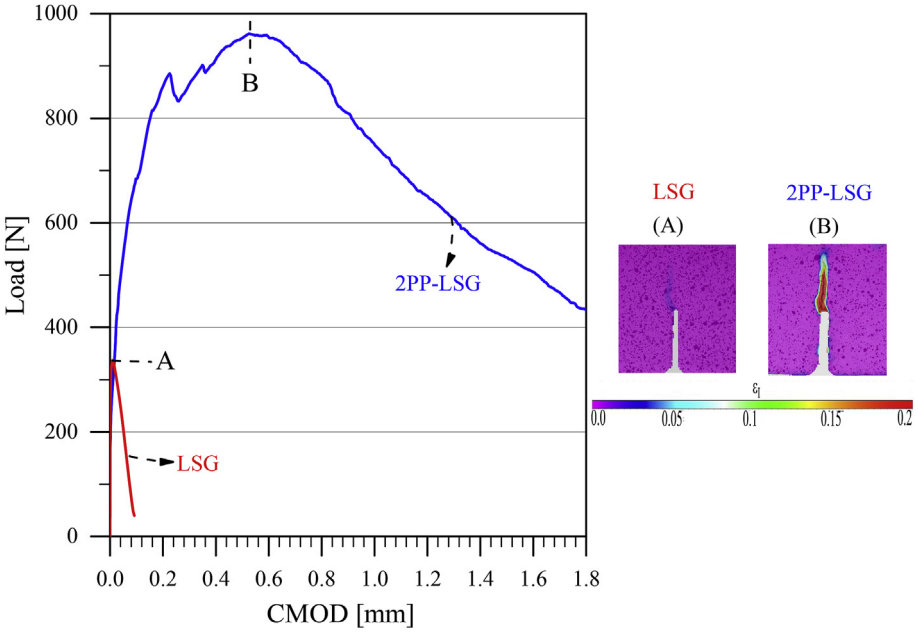

Fig. 7. Fracture toughness tests: representative load vs. CMOD measured by DIC; map of the maximum principal strain (ε_1) captured by DIC at peak load of LSG (A) and 2PP-LSG (B).

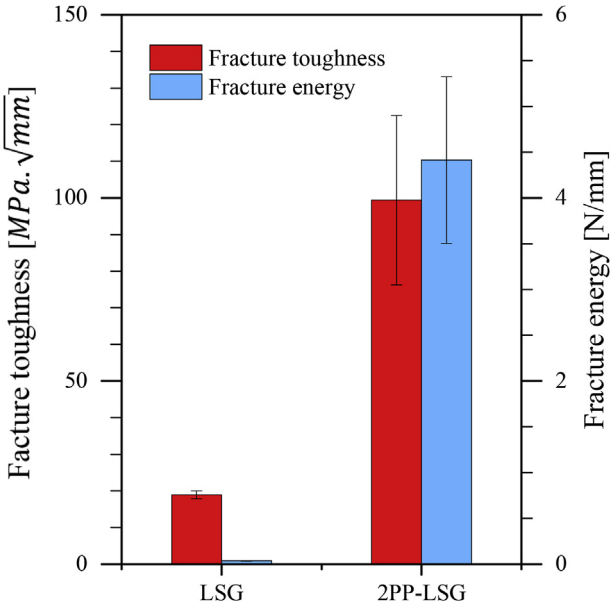

Fig. 8. Fracture toughness tests: fracture energy and fracture toughness at failure.

Compared to the OPC based composite, the basalt fiber reinforced OPC mortar increased the fracture energy by 7.2 times with 5% fiber reinforcement [53]. Moreover, regarding fracture toughness, a maximum increase of 3 times was achieved by using 8.3 wt% of cotton fibers in fly ash based geopolymer [54].

3.2.4. Uniaxial tension

PSH behavior was recorded on HTPP fiber reinforced LSG under uniaxial tension tests. Fig. 9a shows the comparison between the average stress vs. strain curves (continuous lines) of the reinforced and reference materials. The strain was measured by the DIC technique with a virtual strain gage (gage length 80 mm). The reference material indicated a typical stress-strain curve for brittle materials, and the stress dropped immediately after reaching the peak load (approximately 2.3 MPa) with a very small strain. In contrast, the 2PP-LSG exhibited a PSH behavior after the onset of initial crack (at roughly 2 MPa) for a load level higher than 3.1 MPa. The average stress-performance index (i.e., the ratio of the peak of crack bridging stress to the first cracking strength, as detailed in Ref. [10]) of 2PP-LSG, which estimates the ability to perform PSH behavior, was 1.5. In ECC, this index is usually higher than 1.3, as suggested in Ref. [10]. After the initial crack onset, 2PP-LSG indicated a PSH behavior due to a proper load transferring mechanism with an increase in the peak load of 32% in comparison to the initial crack load. The strain capacity was 500 times larger than that of unreinforced material with approximately 1.0% strain. Similar results in literature were reported on OPC cement based ECC using PP fibers [25] or hybrid PP-PVA fibers [55].

The good bridging action allowed the fibers to carry tensile load at the early stage and to reach a higher loading level than that of the plain material. The comparison of average first crack and maximum tensile stress levels is shown in Fig. 9b. The plain material had the same value for the two stress levels, meaning that the crack appeared at the peak tensile load. The 2PP-LSG also exhibited considerable PSH behavior, as demonstrated by the stress-performance index. Furthermore, the tensile strength of the reinforced materials was higher than that of the plain material, with an increase of approximately 18%. However, the initial crack load was lower than that of the reference material. This is consistent with the performance under mode I fracture (Fig. 7) in which the crack appeared early; hence, the HTPP fiber started bridging cracks immediately afterward.

The observation by DIC confirms the PSH behavior of the reinforced composition compared to the reference material. Further inspection of the crack patterns and maximum principal strain maps confirmed the HTPP fibers bridging action in the LSG matrix (Fig. 10). At 0.1% strain in the load direction (Fig. 10a), several cracks appeared on the area of interest, while the initial crack was located on the left side of the sample. In this stage, the HTPP fibers started transferring the applied load back to the LSG matrix, which led to the generation of some new cracks. The micro cracks then propagated and eventually increased strain (see Figs. 9a and 10b) through the load transferring mechanism. Additionally, some new micro cracks were also formed on the sample at the strain of 0.5%. These observations are consistent with DIC observations on fly ash based geopolymer ECC [38]. At the peak load of

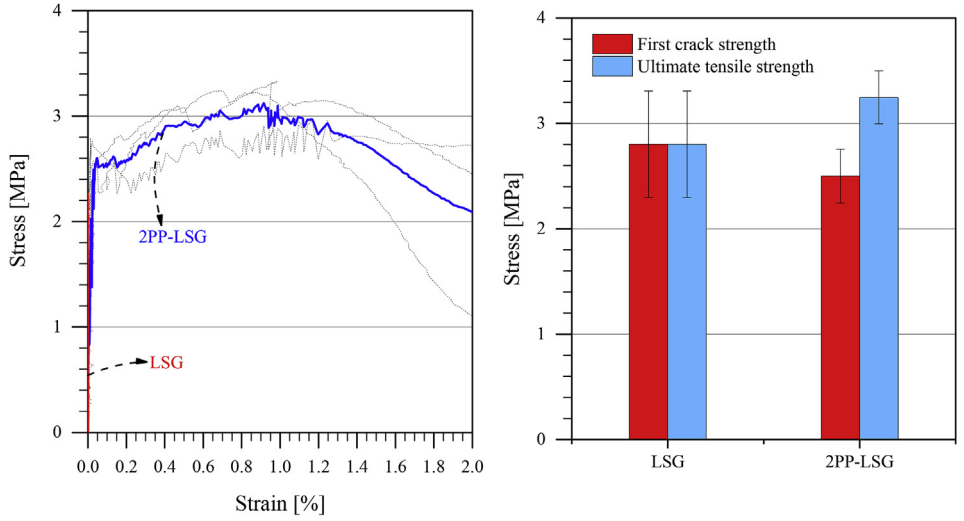

Fig. 9. Tensile test: a) stress-strain measured by DIC (continuous blue line is the average curve, dash line is for individual test) b) first crack and maximum stress levels. (For interpretation of the references to colour in this figure legend, the reader is referred to the Web version of this article.)

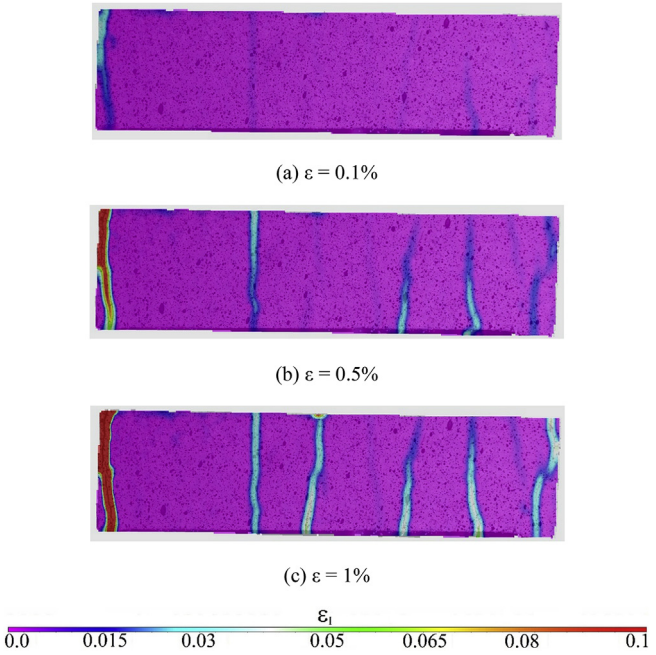

Fig. 10. Tensile test of 2PP-LSG: crack patterns and map of the maximum principal strain (ε_I) recorded by DIC at the strain in the load direction of (a) ε = 0.1%, b) ε = 0.5%, and c) ε = 1%.

2PP-LSG, the strain capacity was approximately 1% (Fig. 10c). Cracks were propagating (started at approximately 2 MPa), while PSH behavior is still observed on the stress vs. strain curve in Fig. 9a. The residual strength at strain 2% is about 70% of peak load, which this indicates residual bonding and friction provided between the HTPP fiber and the LSG matrix.

4. Numerical modeling and comparisons

The numerical simulation by FEM provides some preliminary understandings on the accuracy of an available constitutive model on predicting the mechanical performance of the LSG reinforced with HTPP fiber by comparing to the experimental results under the mode I fracture. The CDP model, generally adopted for ordinary concrete, was exploited. Some parameters of the CDP model (see Section 4.1) were estimated by a preliminary inverse analysis (as in Ref. [56]), calibrating the numerical results in terms of the response registered in the experimental mode I fracture test [57]. The results revealed good agreements between numerical simulation and experimental results. Furthermore, the results highlight the capability of the CDP model to predict the PSH behavior, as recorded via experiments.

4.1. Features of the numerical model

The CDP constitutive model, as available in Ref. [15], was adopted in this investigation to model the nonlinear behavior of the HTPP fiber reinforced LSG. The CDP model combines isotropic linear elasticity and isotropic tensile and compressive plasticity to simulate the inelastic behavior of the considered material. The CDP model considers non-associated potential plastic flow, resulting in a non-symmetric stiffness matrix [15]. The Drucker-Prager hyperbolic function is used to assess the potential flow. The fundamental constitutive parameters of CDP include dilation angle β, plastic potential eccentricity m, stress ratio f_{bo}/f_{co}, (ratio between the compressive strength in biaxial and uniaxial compression, f_{bo} and f_{co}, respectively), shape of the loading surface K, and viscosity parameter V. The parameters β and m represent the shape of the flow potential function and set according to [58] (Table 4). Besides, f_{bo}/f_{co}, and K describe the shape of the yield function, and the adopted values are the recommended default values by Ref. [15] (Table 4). The value of V parameter was assumed to be zero in this analysis.

The uniaxial behavior for the un-cracked material was assumed to be linear. For the cracked state, the compression stress-strain relationship, which was obtained from the experimental testing, was adopted for the CDP model from the average experimental results. For the tensile behavior, inverse analysis was conducted to determine the first

Table 4
Numerical simulation: parameters for CDP model in FEM analysis.

Material	E (MPa)	ν	β	m [a]	f_{bo}/f_{co} [a]	K[a]	σ_u/σ_0	$\varepsilon_u/\varepsilon_0$	G_f (N/mm)
2PP-LSG	2900	0.2	30	1	1.12	0.666	1.51	85.7	0.41

[a] Adopted from Ref. [58].

crack tensile stress σ_0, the maximum stress σ_u, and their corresponding strains ε_0 and ε_u, respectively. Inverse analysis was used to define the unknown parameters simulating the mode I fracture of 2PP-LSG and comparing with the experimental results, as suggested in Refs. [59,60]. Strain hardening behavior, resulting for $\frac{\sigma_u}{\sigma_0} > 1$ and $\frac{\varepsilon_u}{\varepsilon_0} > 1$, was supposed to be for the post cracking state, and the fracture energy G_f was obtained by calculating the underneath stress-strain curve from ε_0 to ε_u. The elastic parameters, Young's modulus and Poisson's ratio, were estimated as 2900 MPa and 0.2, respectively. All parameter inputs of the CDP model are detailed in Table 4.

The 3D numerical simulation reproduced the flexural setup for the notched beam, and the shape and size of the specimen are shown in Fig. 2. Boundary conditions were set to reproduce the two bottom supports and the top applied load on the mid-span. Twenty-node 3D solid hexahedral elements with reduced integration (C3D20R) were used to simulate the model. To assess the mesh dependence of the finite element model, two different mesh sizes with the number of elements of 5160 (coarse mesh) and 17280 (fine mesh) were used. The latter had a refined mesh in the location where relatively high-strain gradients (i.e., cracks) are expected to develop (center of the specimen). All meshes produced almost similar load vs. mid-span deflection relations, while the fine mesh predicts, as expected, a damage evolution and distribution more similar to the experimental one. Accordingly, the fine mesh was supposed for the FEM results presented in the following sections.

4.2. Numerical results and comparison

The preliminary inverse numerical analysis allowed the estimation of the following parameters in the CDP model: σ_u/σ_0, $\varepsilon_u/\varepsilon_0$, and G_f (see Table 4). The inverse analysis was performed to best fit the average experimental results in terms of load vs. mid-span deflection curve of the mode I fracture tests for the reinforced LSG. The parameters were obtained by getting an error lower than 5% (the error less than 10% is acceptable, as reported in Ref. [56]), which was computed by the following:

$$Error = \frac{|A_{exp} - A_{num}|}{A_{exp}} \times 100 \quad (3)$$

where A_{exp} and A_{num} are the areas underneath the experimental and numerical load vs. mid-span deflection curves, respectively.

The experimental and numerical results of flexural loading notched beam are compared in this section in terms of load vs. mid-span deflection and load vs. CMOD. Moreover, the distribution of the maximum principal strain as estimated by FEM and measured by DIC are detailed to show the damage evolution. The evolutions of the mid-span deflection and of the CMOD were compared to the average experimental response (Fig. 11 and Fig. 12a, respectively). Accurate prediction is for the load vs. mid-span deflection both for the initial elastic deformation for the peak load, as well as the post peak branch. The error between experimental and numerical results, according to Equation (3), was roughly 2%.

The numerical analysis proved the PSH behavior observed on the 2PP-LSG through experiments (see Sections 3.2.1 and 3.2.4). The stress performance index $\left(\frac{\sigma_u}{\sigma_0}\right)$ was estimated as 1.51 (Table 4), which is similar to the experimental value (i.e., 1.5).

The numerical prediction of the CMOD had a good agreement with the measured by DIC (see Fig. 12a). The comparison of numerical and experimental load vs. CMOD shows the accuracy of the FEM model both for the initial loading hardening and the softening branches, while an underestimation was for the peak load. In addition, maps of the maximum principal strain by DIC and FEM were captured at the crack initiation load (Fig. 12b, point A) and the peak load (Fig. 12b, point B). The strain distribution recorded numerically precisely detects the crack initiation with the correct maximum principal strain gradient location

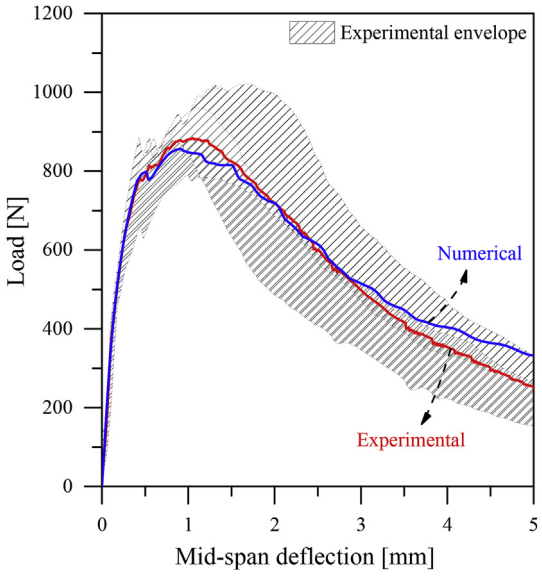

Fig. 11. Comparison of the experimental and numerical results of fracture toughness test: load vs. mid-span deflection.

(Fig. 12b A, bottom), as observed experimentally by DIC (Fig. 12b A, top). Increasing the load level, DIC map shows the crack propagation at the peak load through almost two-thirds of the ligament height. This is also visible on the predicted FEM strain distribution, with highest strain gradient covering the same zone of the crack development. The strain/stress concentrations macroscopically indicate the locations with higher probability of damage occurrence. The prediction of the local effect of fibers reinforcement (e.g., bridging) requires dedicated material models (see e.g., [61]).

5. Conclusions

The investigation demonstrates that ladle slag (LS) can be effectively used as a precursor in cementitious materials. The slag can produce an ettringite-based binder via hydrations with gypsum. Ettringite is the main strength-giving phase of the binder. To deal with the brittleness of the binder, high tenacity polypropylene (HTPP) fiber is employed to produce a high performance fiber reinforced cementitious composite from the waste-based material.

The mechanical properties of the hydrated ladle slag and gypsum (LSG) is significantly improved by using HTPP fiber as reinforcement. The LSG exhibits pseudo strain hardening (PSH) behavior and high ductility with a proper amount and properties of HTPP fibrous reinforcement. In addition, multiple fine cracks along with PSH behavior were observed by the DIC technique under the uniaxial loading condition. The mechanical properties of 2PP-LSG mortars greatly increase by 130%, 40%, 5.30 times, and 124.8 times in flexural, compressive strength, fracture toughness, and fracture energy, respectively after 28 days of curing in water bath.

The use of such fiber reinforced LSG in real applications requires a suitable constitutive model in a predictive design tool. In the present investigation, the concrete damaged plasticity (CDP) model, implemented in a finite element code, was demonstrated to have a good accuracy, setting the proper material parameters. The predicted mode I fracture behavior was in good agreement with the experimental results. However, other in-depth numerical investigations are required to better assess the accuracy of the CDP model with different loading conditions.

Finally, this investigation increases the confidence in the production of high performance fiber reinforced cementitious composites from waste-based matrices reinforced with low-price fibers However, further investigations need addressing, including understanding of the damage

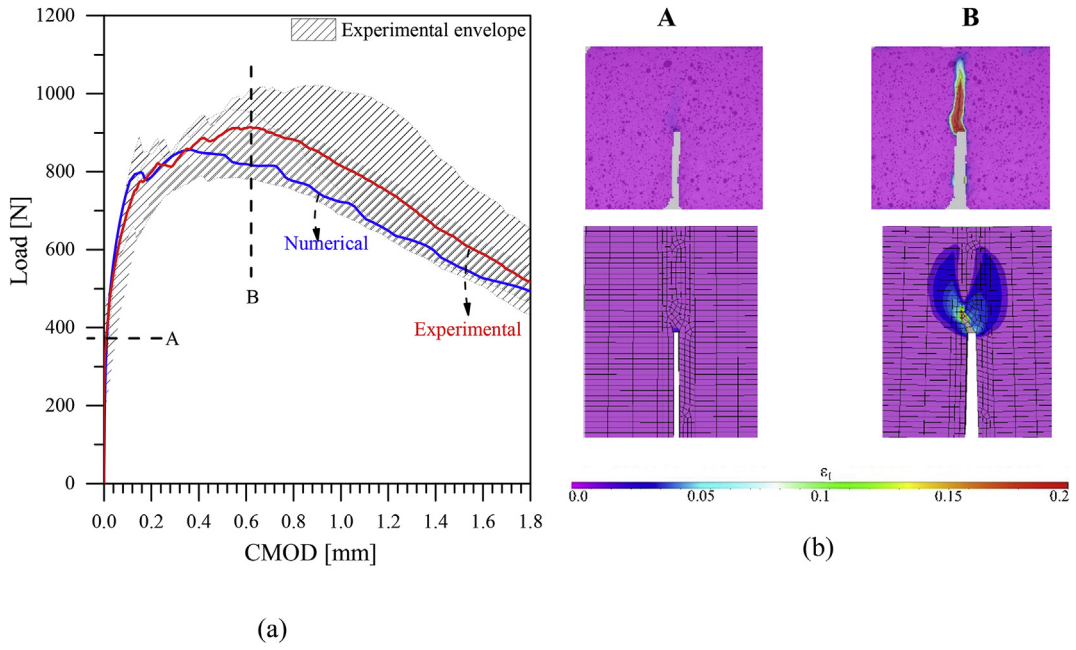

Fig. 12. Comparison between the experimental and numerical results of fracture toughness test: (a) load vs. CMOD, (b) contour of maximum principal strain (ε_1) by DIC (top) and FEM (bottom) at crack initiation load (A - left) and peak load (B - right).

mechanisms with observations at the micro-scale and the durability in aggressive environments.

Acknowledgement

This work was supported by MINSI project [grant number: A70189] under the European Regional Development Fund, European Union. In the University of Oulu, the contributions of Matias Jaskari, Jyri Porter, Kasper Hahtonen, and Tun Tun Nyo to performing the mechanical tests, Thuong Khanh Tran to the calculation of inverse analysis, and Jarno Karvonen to the XRF analysis are gratefully acknowledged. The authors appreciate support from Brasilit Saint-Gobain (Brazil), SSAB Europe Oy (Finland), BASF (Germany), and Vanderbilt (USA) for providing the HTPP fibers, LS, superplasticizer, and dispersing agent, respectively.

References

[1] Steel Statistical Yearbook 2017. Steel Stat Yearb 2010-2017. 2017https://www.worldsteel.org/steel-by-topic/statistics/steel-statistical-yearbook-.html, Accessed date: 7 December 2017.
[2] Yüksel İ. A review of steel slag usage in construction industry for sustainable development. Environ Dev Sustain 2017;19:369–84. https://doi.org/10.1007/s10668-016-9759-x.
[3] Adesanya E, Ohenoja K, Kinnunen P, Illikainen M. Alkali activation of ladle slag from steel-making process. J Sustain Metall 2016:1–11. https://doi.org/10.1007/s40831-016-0089-x.
[4] Natali Murri A, Rickard WDA, Bignozzi MC, van Riessen A. High temperature behaviour of ambient cured alkali-activated materials based on ladle slag. Cement Concr Res 2013;43:51–61. https://doi.org/10.1016/j.cemconres.2012.09.011.
[5] Rungchet A, Chindaprasirt P, Wansom S, Pimraksa K. Hydrothermal synthesis of calcium sulfoaluminate–belite cement from industrial waste materials. J Clean Prod 2016;115:273–83. https://doi.org/10.1016/j.jclepro.2015.12.068.
[6] Magallanes-Rivera RX, Escalante-García JI. Anhydrite/hemihydrate-blast furnace slag cementitious composites: strength development and reactivity. Construct Build Mater 2014;65:20–8. https://doi.org/10.1016/j.conbuildmat.2014.04.056.
[7] Luz CA, Pera J, Cheriaf M, Rocha JC. Behaviour of calcium sulfoaluminate cement in presence of high concentrations of chromium salts. Cement Concr Res 2007;37:624–9. https://doi.org/10.1016/j.cemconres.2006.11.018.
[8] Peysson S, Péra J, Chabannet M. Immobilization of heavy metals by calcium sulfoaluminate cement. Cement Concr Res 2005;35:2261–70. https://doi.org/10.1016/j.cemconres.2005.03.015.
[9] Kim J-M, Choi S-M, Han D. Improving the mechanical properties of rapid air cooled ladle furnace slag powder by gypsum. Construct Build Mater 2016;127:93–101. https://doi.org/10.1016/j.conbuildmat.2016.09.102.
[10] Kanda T, Li VC. Practical design criteria for saturated pseudo strain hardening behavior in ECC. J Adv Concr Technol 2006;4:59–72. https://doi.org/10.3151/jact.4.59.
[11] Li VC, Mishra DK, Wu H-C. Matrix design for pseudo-strain-hardening fibre reinforced cementitious composites. Mater Struct 1995;28:586–95. https://doi.org/10.1007/BF02473191.
[12] Felekoglu B, Tosun-Felekoglu K, Ranade R, Zhang Q, Li VC. Influence of matrix flowability, fiber mixing procedure, and curing conditions on the mechanical performance of HTPP-ECC. Compos B Eng 2014;60:359–70. https://doi.org/10.1016/j.compositesb.2013.12.076.
[13] Jewell RB, Mahboub KC, Robl TL, Bathke AC. Interfacial bond between reinforcing fibers and calcium sulfoaluminate cements: fiber pullout characteristics. ACI Mater J 2015;112:39–48. https://doi.org/10.14359/51687234.
[14] Nguyen H, Carvelli V, Adesanya E, Kinnunen P, Illikainen M. High performance cementitious composite from alkali-activated ladle slag reinforced with polypropylene fibers. Cement Concr Compos 2018;90:150–60. https://doi.org/10.1016/j.cemconcomp.2018.03.024.
[15] SIMULIA. Abaqus/CAE user's guide. 2017.
[16] European Standard. EN 196-1, Methods of testing cement - Part 1: determination of strength. DIN Standards Committee Building and Civil Engineering; 2016.
[17] European standard. EN 450-1, fly ash for concrete. Definition, specifications and conformity criteria. European Standard; 2012.
[18] ISO 13320:2009. Particle size analysis – Laser diffraction methods. International Organization for Standardization; 2009.
[19] Choi S, Kim J-M, Han D, Kim J-H. Hydration properties of ladle furnace slag powder rapidly cooled by air. Construct Build Mater 2016;113:682–90. https://doi.org/10.1016/j.conbuildmat.2016.03.089.
[20] Pelletier L, Winnefeld F, Lothenbach B. The ternary system Portland cement–calcium sulphoaluminate clinker–anhydrite: hydration mechanism and mortar properties. Cement Concr Compos 2010;32:497–507. https://doi.org/10.1016/j.cemconcomp.2010.03.010.
[21] Lanzón M, García-Ruiz PA. Effect of citric acid on setting inhibition and mechanical properties of gypsum building plasters. Construct Build Mater 2012;28:506–11. https://doi.org/10.1016/j.conbuildmat.2011.06.072.
[22] Camarini G, Pinto MCC, Moura AGde, Manzo NR. Effect of citric acid on properties of recycled gypsum plaster to building components. Construct Build Mater 2016;124:383–90. https://doi.org/10.1016/j.conbuildmat.2016.07.112.
[23] Cody AM, Lee H, Cody RD, Spry PG. The effects of chemical environment on the nucleation, growth, and stability of ettringite [Ca3Al(OH)6]2(SO4)3·26H2O. Cement Concr Res 2004;34:869–81. https://doi.org/10.1016/j.cemconres.2003.10.023.
[24] ASTM International. ASTM C191-13, standard test methods for time of setting of hydraulic cement by vicat needle. West Conshohocken, PA: ASTM International; 2013.
[25] Felekoğlu B, Tosun-Felekoğlu K, Gödek E. A novel method for the determination of polymeric micro-fiber distribution of cementitious composites exhibiting multiple cracking behavior under tensile loading. Construct Build Mater 2015;86:85–94. https://doi.org/10.1016/j.conbuildmat.2015.03.094.
[26] Nematollahi B, Sanjayan J, Shaikh FUA. Matrix design of strain hardening fiber reinforced engineered geopolymer composite. Compos B Eng 2016;89:253–65. https://doi.org/10.1016/j.compositesb.2015.11.039.
[27] Winnefeld F, Lothenbach B. Hydration of calcium sulfoaluminate cements — experimental findings and thermodynamic modelling. Cement Concr Res

2010;40:1239–47. https://doi.org/10.1016/j.cemconres.2009.08.014.
[28] Gruskovnjak A, Lothenbach B, Winnefeld F, Münch B, Figi R, Ko S-C, et al. Quantification of hydration phases in supersulfated cements: review and new approaches. Adv Cement Res 2011;23:265–75. https://doi.org/10.1680/adcr.2011.23.6.265.
[29] da Costa EB, Rodríguez ED, Bernal SA, Provis JL, Gobbo LA, Kirchheim AP. Production and hydration of calcium sulfoaluminate-belite cements derived from aluminium anodising sludge. Construct Build Mater 2016;122:373–83. https://doi.org/10.1016/j.conbuildmat.2016.06.022.
[30] Choi J-I, Lee BY, Ranade R, Li VC, Lee Y. Ultra-high-ductile behavior of a polyethylene fiber-reinforced alkali-activated slag-based composite. Cement Concr Compos 2016;70:153–8. https://doi.org/10.1016/j.cemconcomp.2016.04.002.
[31] Lee BY, Cho C-G, Lim H-J, Song J-K, Yang K-H, Li VC. Strain hardening fiber reinforced alkali-activated mortar – a feasibility study. Non Destr Tech Assess Concr 2012;37:15–20. https://doi.org/10.1016/j.conbuildmat.2012.06.007.
[32] LaVision StrainMaster 2016. http://www.lavision.de/en/products/strainmaster/index.php (accessed January 27, 2017).
[33] Correlated Solutions – VIC-2D™2016. http://correlatedsolutions.com/vic-2d/(accessed March 15, 2017).
[34] ISO 679:2009. Cement – test methods – determination of strength. International Organization for Standardization; 2009.
[35] RILEM. Determination of the fracture energy of mortar and concrete by means of three-point bend tests on notched beams. Mater Struct 1985;18:287–90. https://doi.org/10.1007/BF02472918.
[36] Karihaloo BL, Nallathambi P. Effective crack model for the determination of fracture toughness (KIce) of concrete. Eng Fract Mech 1990;35:637–45. https://doi.org/10.1016/0013-7944(90)90146-8.
[37] JSCE. Recommendations for design and construction of high performance fiber reinforced cement composites with multiple fine cracks. Concr. Eng. Ser. 2008;82. Japan: JSCE.
[38] Ohno M, Li VC. A feasibility study of strain hardening fiber reinforced fly ash-based geopolymer composites. Construct Build Mater 2014;57:163–8. https://doi.org/10.1016/j.conbuildmat.2014.02.005.
[39] Ranjbar N, Talebian S, Mehrali M, Kuenzel C, Cornelis Metselaar HS, Jumaat MZ. Mechanisms of interfacial bond in steel and polypropylene fiber reinforced geopolymer composites. Compos Sci Technol 2016;122:73–81. https://doi.org/10.1016/j.compscitech.2015.11.009.
[40] Puertas F, Amat T, Fernández-Jiménez A, Vázquez T. Mechanical and durable behaviour of alkaline cement mortars reinforced with polypropylene fibres. Cement Concr Res 2003;33:2031–6. https://doi.org/10.1016/S0008-8846(03)00222-9.
[41] Corinaldesi V, Nardinocchi A. Influence of type of fibers on the properties of high performance cement-based composites. Construct Build Mater 2016;107:321–31. https://doi.org/10.1016/j.conbuildmat.2016.01.024.
[42] Toutanji HA. Properties of polypropylene fiber reinforced silica fume expansive-cement concrete. Construct Build Mater 1999;13:171–7. https://doi.org/10.1016/S0950-0618(99)00027-6.
[43] Felekoğlu B, Tosun-Felekoğlu K, Keskinateş M, Gödek E. A comparative study on the compatibility of PVA and HTPP fibers with various cementitious matrices under flexural loads. Construct Build Mater 2016;121:423–8. https://doi.org/10.1016/j.conbuildmat.2016.06.004.
[44] Mastali M, Valente IB, Barros JAO. Flexural performance of innovative hybrid sandwich panels with special focus on the shear connection behavior. Compos Struct 2017;160:100–17. https://doi.org/10.1016/j.compstruct.2016.10.066.
[45] Zhu H, Yan M, Wang P, Li C, Cheng Y. Mechanical performance of concrete combined with a novel high strength organic fiber. Construct Build Mater 2015;78:289–94. https://doi.org/10.1016/j.conbuildmat.2015.01.014.
[46] Afroughsabet V, Biolzi L, Ozbakkaloglu T. High-performance fiber-reinforced concrete: a review. J Mater Sci 2016;51:6517–51. https://doi.org/10.1007/s10853-016-9917-4.
[47] Mastali M, Dalvand A, Sattarifard AR, Abdollahnejad Z, Illikainen M. Characterization and optimization of hardened properties of self-consolidating concrete incorporating recycled steel, industrial steel, polypropylene and hybrid fibers. Compos B Eng 2018;151:186–200. https://doi.org/10.1016/j.compositesb.2018.06.021.
[48] Li VC. A simplified micromechanical model of compressive strength of fiber-reinforced cementitious composites. Spec Issue Micromechanics Fail Cem Compos 1992;14:131–41. https://doi.org/10.1016/0958-9465(92)90006-H.
[49] Janotka I, Krajči L, Ray A, Mojumdar S. The hydration phase and pore structure formation in the blends of sulfoaluminate-belite cement with Portland cement. Cement Concr Res 2003;33:489–97. https://doi.org/10.1016/S0008-8846(02)00994-8.
[50] García-Maté M, De la Torre AG, León-Reina L, Losilla ER, Aranda MAG, Santacruz I. Effect of calcium sulfate source on the hydration of calcium sulfoaluminate eco-cement. Cement Concr Compos 2015;55:53–61. https://doi.org/10.1016/j.cemconcomp.2014.08.003.
[51] Hu C, Hou D, Li Z. Micro-mechanical properties of calcium sulfoaluminate cement and the correlation with microstructures. Cement Concr Compos 2017;80:10–6. https://doi.org/10.1016/j.cemconcomp.2017.02.005.
[52] Nguyen H, Carvelli V, Fujii T, Okubo K. Cement mortar reinforced with reclaimed carbon fibres, CFRP waste or prepreg carbon waste. Construct Build Mater 2016;126:321–31. https://doi.org/10.1016/j.conbuildmat.2016.09.044.
[53] Fenu L, Forni D, Cadoni E. Dynamic behaviour of cement mortars reinforced with glass and basalt fibres. Compos B Eng 2016;92:142–50. https://doi.org/10.1016/j.compositesb.2016.02.035.
[54] Alomayri T, Shaikh FUA, Low IM. Synthesis and mechanical properties of cotton fabric reinforced geopolymer composites. Compos B Eng 2014;60:36–42. https://doi.org/10.1016/j.compositesb.2013.12.036.
[55] Pakravan HR, Jamshidi M, Latifi M. Study on fiber hybridization effect of engineered cementitious composites with low- and high-modulus polymeric fibers. Construct Build Mater 2016;112:739–46. https://doi.org/10.1016/j.conbuildmat.2016.02.112.
[56] Mastali M, Valente IB, Barros JAO. Development of innovative hybrid sandwich panel slabs: advanced numerical simulations and parametric studies. Compos Struct 2016;152:362–81. https://doi.org/10.1016/j.compstruct.2016.05.072.
[57] Pereira Eduardo NB, Barros Joaquim AO, Camões Aires. Steel fiber-reinforced self-compacting concrete: experimental research and numerical simulation. J Struct Eng 2008;134:1310–21. https://doi.org/10.1061/(ASCE)0733-9445(2008)134:8(1310).
[58] Jankowiak T, Łodygowski T. Identification of parameters of concrete damage plasticity constitutive model. Found Civ Environ Eng 2005;6:53–69.
[59] Kheradmand M, Mastali M, Abdollahnejad Z, Pacheco-Torgal F. Experimental and numerical investigations on the flexural performance of geopolymers reinforced with short hybrid polymeric fibres. Compos B Eng 2017;126:108–18. https://doi.org/10.1016/j.compositesb.2017.06.001.
[60] Enfedaque A, Alberti MG, Gálvez JC, Domingo J. Numerical simulation of the fracture behaviour of glass fibre reinforced cement. Construct Build Mater 2017;136:108–17. https://doi.org/10.1016/j.conbuildmat.2016.12.130.
[61] Yang E-H, Wang S, Yang Y, Li VC. Fiber-bridging constitutive law of engineered cementitious composites. J Adv Concr Technol 2008;6:181–93. https://doi.org/10.3151/jact.6.181.